Distinct neocortical and entorhinal networks for time, space, and reward

John B. Issa and Daniel A. Dombeck
Department of Neurobiology, Northwestern University

Abstract
Variables relevant to behavior and cognition are often synthesized via computations that combine external cues and internal states. Especially salient and ubiquitous among these variables are time, space, and reward, but how they are simultaneously represented throughout the neocortex and the entorhinal cortex is not well understood. Here, we devised a behavioral task in virtual reality that includes timing, navigation, and reward components and, using a multifocus microscope that permits simultaneous mesoscopic Ca^{2+} imaging of neocortex and entorhinal cortex, we uncover dedicated and distinct subnetworks for interval timing, spatial navigation, and reward. Interestingly, the timing subnetwork includes a strong contribution from barrel cortex, pointing towards a previously unknown role for this cortex in interval timing.

Introduction
The neocortex handles a diversity of information streams[1]. For example, unimodal sources of information such as vision, touch, or movement are represented in the neocortical primary sensory and motor regions. However, variables relevant to behavior and cognition are often not explicitly represented in these signals and instead must be synthesized within the brain via computations that combine external cues and internal states[2,3]. Variables such as time, reward state, and spatial position may be especially relevant to decision-making and memory[4]. We wished to determine which brain regions are involved in representing these variables, with a particular focus on regions of the neocortex and the entorhinal cortex, which connects the neocortex with the hippocampus[5]. Thus, we devised a behavioral task in virtual reality that serves to isolate the aforementioned variables of time, reward state, and spatial position and, using a custom-built microscope, we performed multifocus mesoscale Ca^{2+} imaging across much of the neocortex along with the entorhinal cortex, allowing us to ask if and how these regions may be involved in coding for time, reward, and spatial position.

Results
We utilized a task that engages three different aspects of behavior: reward, spatial navigation, and interval timing[6] (Figure 1A). Head-fixed mice ran on a linear treadmill to traverse a 3.1-m virtual track. A water reward was delivered at the end of the track, followed 4 seconds later by teleportation back to the start of the track. The timing portion of the task was achieved by placing a door halfway down the track where mice need to stop running for the target duration (typically 6 seconds), at which point the door opens and the mice can proceed down the track. However, if they resume running before the target time, the timer resets until the next attempt at running. Once mice learned the task, the door was made invisible so that no cues about the timing interval were explicitly provided. Wait times in well-trained mice follow a normal distribution with a mean slightly below the target time, likely reflecting information gathering and optimal foraging[7]. Importantly, the timing portion of the task requires the mouse to stand still on the treadmill for the target waiting time; thus, while some motor behaviors could still be ongoing, large movements and outright running are eliminated, potentially helping isolate timing signals that would otherwise be overwhelmed by velocity-related signals in the neocortex[8].

Given that the entorhinal cortex may be involved in interval timing[6,9–11], we wished to record signals from the entorhinal cortex and multiple cortical areas (including visual, somatosensory, and motor cortices) during this behavior. We chose to use transcranial mesoscale Ca^{2+} imaging since this method can accommodate a large imaging field[12]. The low temporal resolution (on the order of hundreds of milliseconds) is acceptable for our task since task-relevant timescales are on the order of seconds. We used a transgenic GCaMP6s mouse with high expression levels throughout neocortex and entorhinal cortex[13]. To image the entorhinal cortex simultaneously, we developed a hybrid preparation that combines an implanted microprism (1.5 or 2 mm^2) over the entorhinal cortex[14] along with a transcranial

clear skull preparation for dorsal neocortex covered by an 8 mm^2 coverslip. The imaging planes for these two windows are offset by ~3 mm. To achieve simultaneous in-focus imaging of both regions, we built a multifocus fluorescence microscope (Figure 1B). Using two imaging paths leading to two separate cameras, we manually adjusted the back focal length of the second camera, allowing us independent control of the focal planes of the two cameras. Two LEDs (470 nm and 405 nm) were alternatively pulsed, allowing correction for hemodynamic changes[15].

Typical imaging sessions lasted 20-30 minutes, during which trained mice successfully completed ~30 laps. Individual imaging fields were registered to bregma and normalized to bregma-lambda distance. Fluorescence traces from seven exemplar 0.1 x 0.1 mm^2 superpixels are shown for a 2-minute stretch of an imaging session (Figure 2), along with task-relevant behaviors of treadmill velocity, licking, and position on the virtual track. Each of these signals is averaged across trials for three aspects of the task: first, timing at the door, which is formed by normalizing time to the duration from the start to the end of the timing period; second, time to reward, which is aligned to the time of reward delivery and followed after 4 seconds by teleportation to the start of the track; third, track position, which spans the 3.1-m track distance and, at each 1-cm bin, averages across any times when the mouse is moving down the track. The signals differ across pixels, with differing preferences for each task component and variation in the waveforms for each.

To explore these differences more systematically, we sought a method that would allow us to combine results across mice and, through dimensionality reduction, uncover a small number of components that are sufficient to explain a large amount of the variance in the fluorescence signals. With this goal in mind, we developed a group-wise non-negative matrix factorization algorithm[16] (Figure 3A). For each pixel from each imaging session, we formed a single vector by concatenating the trial-averaged signals for timing, reward, and track position. This vector has a length of 794 data points. Then we formed a matrix for all 36318 pixels across 9 imaging sessions, where each row is the trial-averaged vector for that pixel, resulting in a 36318 x 794 matrix X.

We chose the number of components to be seven, based on the elbow in variance explained as we increased the number of components (Figure 3B). Applying non-negative matrix factorization to X, we uncovered seven components, each of which has one row in the temporal matrix H (length 794) and one column in the weight matrix W (length 36318), the latter of which can be used to form 2D spatial maps for individual sessions (Figure 3C-E). Applying W to an individual session's full movie F (which has 43432 time points and 3968 pixels) allows us to compress the data to seven dimensions (43432 x 7), where each dimension corresponds to one component. Then, using the same weights, we can calculate an estimate of the full movie, F'. This recovered movie produces a good fit of the original movie, explaining 94% of the variance in the traces, nearly identical to factorization using PCA, thus indicating that non-negative matrix factorization is optimally capturing variance with a low number of components (Figure 3C). Note that this factorization does not use any information about where each pixel came from, nor the temporal order of the individual points within the trail-averaged vectors. Therefore, it is notable that the individual components are temporally and spatially smooth, and the spatial maps are typically symmetric for individual mice (left-right symmetry). More impressively, the spatial maps are highly similar across different sessions, quantified by measuring the spatial correlation between each pair of sessions for same ('within component') and different ('across components') components. (Figure 3F). To form a unified map that may highlight which regions are active for each different behavior, we averaged across components that are most active during navigation, timing, or reward (Figure 3G), which include, for navigation: retrosplenial, visual, and lower limb somatosensory cortices along with some activation in primary and secondary motor cortices; for timing: barrel cortex and a focal region of secondary motor cortex; for reward, much of primary and secondary motor cortex. Within entorhinal cortex, the picture is mixed, with all components contributing but with spatial heterogeneity within the ~2 mm^2 area imaged through the microprism.

How do these components correspond to the known functional specializations of these regions? Along with their respective temporal vectors as found in the rows of H, we can take the seven recovered projections in time (Y) and examine how each component correlates to other aspects of behavior not explicitly used in forming the matrix X, such as whisking, running, and pupil diameter. We formed a basis set of predictors using time relative to the door start and stop, time relative to reward delivery, and finally variables related to movement as recorded by the treadmill velocity and a face camera, which captured sniffing, whisking, and pupil diameter (Figure 4A). Note that track position was not included in these predictors. Next, using non-negative ridge regression with 10-fold cross-validation, we found weights for these predictors. The reconstructed signals Y' using this approach provided an efficient method of approximating the original movie using a low-dimensional projection (Figure 4B), with the reconstructed estimate of the full movie F'' (formed by multiplying Y' by the weights W) explaining 77% of the variance in F. This approach captures similar trends as seen in the temporal vectors for the components as shown in Figure 3D for timing and reward but also serves both to separate contributions from co-mingled variables (such as deceleration and reward approach) and to parcel out contributions from different dimensions of motor activity (Figure 4C). Some of the resulting weights are as expected. For example, components 2 and 4, which have strong weights in visual cortex (Figure 3E), have stronger weights in the regression for optic flow than for any direct measure of treadmill velocity (Figure 4C). Component 3, which has strong weights in somatomotor cortices (Figure 3E) and closely tracks treadmill velocity (Figure 4B), reassuringly has a strong weight in the regression for running (Figure 4C). Component 7 is particularly interesting. It would be reasonable to predict that its activation during waits at the door, as reflected in its temporal vector (Figure 3D), would be explained by another variable, such as ongoing whisking or changes in arousal[21]; however, at least for the movement variables we measured, none of them showed up with strong weights in the regression and instead most of the weights came from the door basis set itself (Figure 4C). Thus, the temporal vectors appear to capture relevant aspects of the behavior for the regions to which they correspond.

Discussion

A challenge in ascertaining the functional specialization of any brain region is choosing stimuli and behaviors that optimally engage that brain region. Further, representations of these variables will depend heavily on the task the animal is engaged in[22]. While the behaviors tested here are certainly not comprehensive, the incorporation of a timing task along with spatial navigation and reward helps to engage and isolate multiple dimensions of behavior. Using this approach, we find that distinct regions of neocortex and entorhinal cortex are highly engaged across timing, reward, and navigation. These form potential subnetworks, which are distributed but dedicated for certain dimensions of a task. This finding is in agreement with other studies that have found that many regions of neocortex are not just multi-modal, they are also multi-purpose. For example, neurons in visual[17], somatosensory[18], and other cortices[19] can represent spatial position, and neurons in various regions of cortex can represent time[6,9,20]. Whether and how neurons across regions may work together to track time, reward expectation, or spatial position is not answered by the present study, but our results are consistent with the idea that multiple regions of cortex work together to generate and maintain representations of behaviorally relevant variables.

The identification of a timing subnetwork, which is broadly distributed across much of neocortex and entorhinal cortex, was facilitated by using a behavioral task that requires an interval to be timed explicitly. Further, this timing period requires the mouse to be stationary, which helps isolate timing-related signals from motor-related signals[8]. Surprisingly, the components identified by non-negative factorization revealed that the barrel cortex was a major contributor during timing. This correlation was not explained by an increase in whisking during the timing period. One fascinating possibility is that the intrinsic timing circuits that drive rhythmic whisking[23] could be repurposed to help measure time intervals in trained mice. Future work will be needed to see if this speculation is indeed true. Nonetheless, our results are consistent with functional specializations for timing, spatial navigation, and reward across the neocortex, and these representations may then be communicated via the entorhinal cortex to the hippocampus and other brain regions to inform memory and behavior.

Methods

All animal procedures were approved by the Northwestern University Institutional Animal Care and Use Committee. Mice expressing GCaMP6s were generated by crossing tetO-GCaMP6s mice (JAX No. 024742) with Camk2a-tTA mice (JAX No. 007004)[13].

Surgery

Microprism implants for medial and lateral entorhinal cortex were performed as described previously[14]. Window for transcranial imaging of dorsal neocortex was formed by applying multiple layers of superglue, such as Norland 81, and a large coverslip (either 8 mm square or 10 mm round) placed above. A custom titanium headplate was then affixed using dental cement. Mice were allowed up to a week to recover before starting on water restriction (1 mL per day).

Behavior

Mice were first habituated to head fixation and running on a linear treadmill. Water rewards were delivered at the end of a 3.1-m virtual track. Daily sessions lasted 40-60 minutes. Once mice ran at least 2 laps per minute, the door stop was introduced, as previously described[6]. Mice were required to reach the door and stop running for a given target interval (initially 1.5 or 2 s) before the door would open, allowing them to continue to the end of the track to receive the water reward. If mice started running before the target interval, the door remained closed and the timer was reset until the next stop attempt. Once mice achieved at least 1 lap per minute, the target interval was increased. For initial training, the door was visible, thus providing a visual cue once the target interval was reached. However, eventually the door was made invisible, requiring the mice to rely completely on an internal clock. Fully trained mice would achieve 1 lap per minute for a 6-s target interval with the invisible door. One to two months of training was typically required before mice reached this level of training.

Multifocus Microscope, Imaging, and Hardware

A 50:50 beamsplitter on the emission path split the image to a pair of tube lenses. Distance from each tube lens to each camera was independently controlled. For small deviations, the relationship between the back focal length L (tube lens to camera) and working distance D (objective to imaging plane) can be approximated as $L*D = C$, where C is a constant that depends on the optics being used. For our purposes, $C = 3300\ mm^2$. For small deviations near the optimal focal length L, deviations in D are approximately the same but in the opposite direction. Thus, for L = 60 mm, D = 55 mm. For L = 57.4 mm, D = 57.5 mm. Adjusting the back focal length also introduces changes in the magnification, so that decreasing L will increase D and decrease the magnification[24]. But this change in magnification is minimal for small changes in the back focal length. Using this strategy, each camera could be independently focused to a different working distance.

Camera 1 (Photometrics Prime BSI Express) was used as the master, running with an exposure time of 17 msec. Excitation was provided by a pair of LEDs, centered at 470 nm and 405 nm, which were alternatively turned on by a custom-built flip-flop circuit driven by the frame sync from camera 1. Camera 2 was triggered by the frame sync from camera 1, so both cameras ran at 60 Hz while the LEDs pulsed at 30 Hz. Camera 3 was triggered by the same signal that drove the 470 nm LED, so it ran at 30 Hz. All camera and LED times were sent as TTL pulses to an NI-DAQ along with other behavioral data (treadmill velocity, lick sensor data, reward pulses), allowing synchronization of all relevant signals. The collection of data and virtual reality environment were programmed in MATLAB using ViRMEn[25] and custom scripts.

Image Processing

For rigid registration across sessions and mice, bregma and lambda were manually chosen from a fluorescence image for each session. A vasculature mask was generated by thresholding for low intensity pixels, and these pixels were subsequently ignored. Images were then downsampled to 0.1 x 0.1 mm^2 superpixels. Fluorescence traces for 470 nm and 405 nm illumination were formed for each

superpixel, and a corrected signal F_C (t) was calculated by subtracting the dark current and then dividing the 470 nm signal by the 405 nm signal. The baseline $F_0(t)$ was approximated by estimating weights of a basis set of slowly varying exponentials and sinusoids, allowing calculation of $\Delta F/F_0$. Next, spatial maps were deblurred using a Lucy-Richardson deconvolution with a σ = 500 μm point spread function[26,27]. Finally, signals were deconvolved[28] using a double exponential (80 msec rise tau, 500 msec decay tau) to recover an estimate of firing rates.

Analysis

Non-negative matrix factorization was performed using the function nnmf in MATLAB. Non-negative ridge regression was performed using a custom-written script in MATLAB. Quadratic programming with quadprog was used to speed computation of the regression.

References

1. Marr, D. (1997). A theory for cerebral neocortex. Proceedings of the Royal Society of London. Series B. Biological Sciences *176*, 161–234. https://doi.org/10.1098/rspb.1970.0040.
2. Wang, X.-J. (2022). Theory of the Multiregional Neocortex: Large-Scale Neural Dynamics and Distributed Cognition. Annual Review of Neuroscience *45*, 533–560. https://doi.org/10.1146/annurev-neuro-110920-035434.
3. Mountcastle, V.B. (1997). The columnar organization of the neocortex. Brain *120*, 701–722. https://doi.org/10.1093/brain/120.4.701.
4. Eichenbaum, H. (2017). On the Integration of Space, Time, and Memory. Neuron *95*, 1007–1018. https://doi.org/10.1016/j.neuron.2017.06.036.
5. Witter, M.P., Doan, T.P., Jacobsen, B., Nilssen, E.S., and Ohara, S. (2017). Architecture of the Entorhinal Cortex A Review of Entorhinal Anatomy in Rodents with Some Comparative Notes. Front Syst Neurosci *11*. https://doi.org/10.3389/fnsys.2017.00046.
6. Heys, J.G., and Dombeck, D.A. (2018). Evidence for a subcircuit in medial entorhinal cortex representing elapsed time during immobility. Nat. Neurosci. *21*, 1574–1582. https://doi.org/10.1038/s41593-018-0252-8.
7. Stephens, D.W., and Krebs, J.R. (1986). Foraging Theory (Princeton University Press).
8. Musall, S., Kaufman, M.T., Juavinett, A.L., Gluf, S., and Churchland, A.K. (2019). Single-trial neural dynamics are dominated by richly varied movements. Nature Neuroscience *22*, 1677–1686. https://doi.org/10.1038/s41593-019-0502-4.
9. Tsao, A., Sugar, J., Lu, L., Wang, C., Knierim, J.J., Moser, M.-B., and Moser, E.I. (2018). Integrating time from experience in the lateral entorhinal cortex. Nature *561*, 57–62. https://doi.org/10.1038/s41586-018-0459-6.
10. Kanter, B.R., Lykken, C.M., Polti, I., Moser, M.-B., and Moser, E.I. (2025). Event structure sculpts neural population dynamics in the lateral entorhinal cortex. Science *388*, eadr0927. https://doi.org/10.1126/science.adr0927.
11. Heys, J.G., Wu, Z., Allegra Mascaro, A.L., and Dombeck, D.A. (2020). Inactivation of the Medial Entorhinal Cortex Selectively Disrupts Learning of Interval Timing. Cell Reports *32*, 108163. https://doi.org/10.1016/j.celrep.2020.108163.
12. Ma, Y., Shaik, M.A., Kim, S.H., Kozberg, M.G., Thibodeaux, D.N., Zhao, H.T., Yu, H., and Hillman, E.M.C. (2016). Wide-field optical mapping of neural activity and brain haemodynamics: considerations and novel approaches. Philosophical Transactions of the Royal Society B: Biological Sciences *371*, 20150360. https://doi.org/10.1098/rstb.2015.0360.
13. Wekselblatt, J.B., Flister, E.D., Piscopo, D.M., and Niell, C.M. (2016). Large-scale imaging of cortical dynamics during sensory perception and behavior. Journal of Neurophysiology, jn.01056.2015. https://doi.org/10.1152/jn.01056.2015.
14. Issa, J.B., Radvansky, B.A., Xuan, F., and Dombeck, D.A. (2024). Lateral entorhinal cortex subpopulations represent experiential epochs surrounding reward. Nat Neurosci *27*, 536–546. https://doi.org/10.1038/s41593-023-01557-4.
15. Valley, M.T., Moore, M.G., Zhuang, J., Mesa, N., Castelli, D., Sullivan, D., Reimers, M., and Waters, J. (2020). Separation of hemodynamic signals from GCaMP fluorescence measured with wide-field imaging. Journal of Neurophysiology *123*, 356–366. https://doi.org/10.1152/jn.00304.2019.
16. Lee, D.D., and Seung, H.S. (1999). Learning the parts of objects by non-negative matrix factorization. Nature *401*, 788–791. https://doi.org/10.1038/44565.
17. Saleem, A.B., Diamanti, E.M., Fournier, J., Harris, K.D., and Carandini, M. (2018). Coherent encoding of subjective spatial position in visual cortex and hippocampus. Nature *562*, 124. https://doi.org/10.1038/s41586-018-0516-1.
18. Long, X., and Zhang, S.-J. (2021). A novel somatosensory spatial navigation system outside the hippocampal formation. Cell Res *31*, 649–663. https://doi.org/10.1038/s41422-020-00448-8.

19. Esteves, I.M., Chang, H., Neumann, A.R., Sun, J., Mohajerani, M.H., and McNaughton, B.L. (2021). Spatial Information Encoding across Multiple Neocortical Regions Depends on an Intact Hippocampus. J. Neurosci. *41*, 307–319. https://doi.org/10.1523/JNEUROSCI.1788-20.2020.
20. Tiganj, Z., Cromer, J.A., Roy, J.E., Miller, E.K., and Howard, M.W. (2018). Compressed Timeline of Recent Experience in Monkey Lateral Prefrontal Cortex. J Cogn Neurosci *30*, 935–950. https://doi.org/10.1162/jocn_a_01273.
21. Raut, R.V., Rosenthal, Z.P., Wang, X., Miao, H., Zhang, Z., Lee, J.-M., Raichle, M.E., Bauer, A.Q., Brunton, S.L., Brunton, B.W., et al. (2025). Arousal as a universal embedding for spatiotemporal brain dynamics. Nature, 1–8. https://doi.org/10.1038/s41586-025-09544-4.
22. Pinto, L., Rajan, K., DePasquale, B., Thiberge, S.Y., Tank, D.W., and Brody, C.D. (2019). Task-Dependent Changes in the Large-Scale Dynamics and Necessity of Cortical Regions. Neuron *104*, 810-824.e9. https://doi.org/10.1016/j.neuron.2019.08.025.
23. Takatoh, J., Prevosto, V., Thompson, P.M., Lu, J., Chung, L., Harrahill, A., Li, S., Zhao, S., He, Z., Golomb, D., et al. (2022). The whisking oscillator circuit. Nature *609*, 560–568. https://doi.org/10.1038/s41586-022-05144-8.
24. Demuro, A., and Parker, I. (2008). Multi-dimensional resolution of elementary Ca2+ signals by simultaneous multi-focal imaging. Cell Calcium *43*, 367–374. https://doi.org/10.1016/j.ceca.2007.07.002.
25. Aronov, D., and Tank, D.W. (2014). Engagement of Neural Circuits Underlying 2D Spatial Navigation in a Rodent Virtual Reality System. Neuron *84*, 442–456. https://doi.org/10.1016/j.neuron.2014.08.042.
26. Lucy, L.B. (1974). An iterative technique for the rectification of observed distributions. The Astronomical Journal *79*, 745. https://doi.org/10.1086/111605.
27. Issa, J.B., Haeffele, B.D., Agarwal, A., Bergles, D.E., Young, E.D., and Yue, D.T. (2014). Multiscale optical Ca2+ imaging of tonal organization in mouse auditory cortex. Neuron *83*, 944–959. https://doi.org/10.1016/j.neuron.2014.07.009.
28. Friedrich, J., Zhou, P., and Paninski, L. (2017). Fast online deconvolution of calcium imaging data. PLOS Computational Biology *13*, e1005423. https://doi.org/10.1371/journal.pcbi.1005423.
29. Wang, Q., Ding, S.-L., Li, Y., Royall, J., Feng, D., Lesnar, P., Graddis, N., Naeemi, M., Facer, B., Ho, A., et al. (2020). The Allen Mouse Brain Common Coordinate Framework: A 3D Reference Atlas. Cell *181*, 936-953.e20. https://doi.org/10.1016/j.cell.2020.04.007.

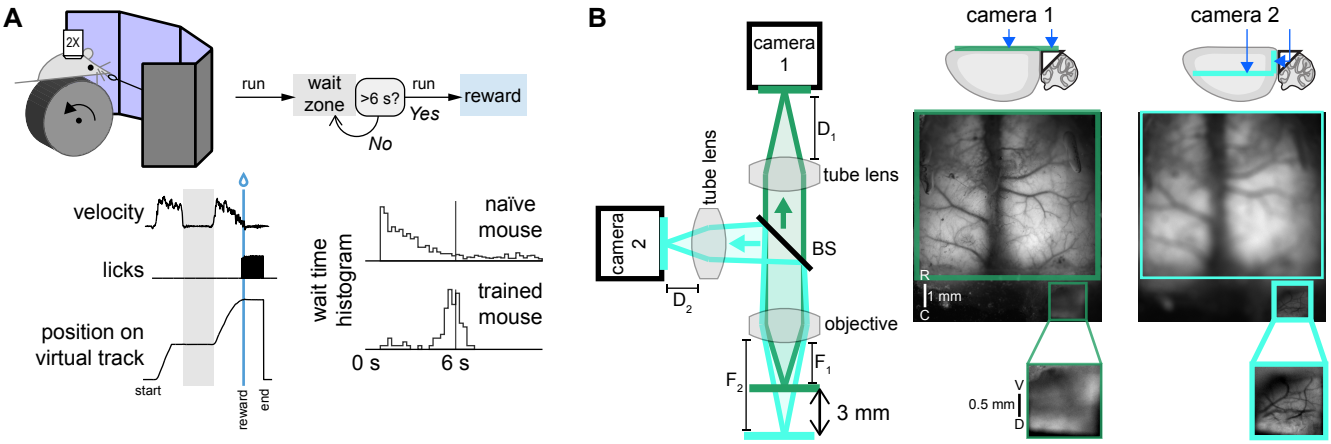

Figure 1. Behavior and imaging setup

A) Mice learn a VR task with three components: 1) they run on a treadmill to travel down a 3.1 m virtual track; 2) they receive a reward at the end of the track; 3) halfway down the track, there is an invisible door, where they learn to stop running and wait for at least 6 seconds before they can continue running to the end of the track. In trained mice, the histogram of wait times at the door is normally distributed with a mean near the target time of 6 seconds.

B) Multifocus microscope for multiplane imaging. Two imaging collection paths (formed by 50:50 beamsplitter, BS) go to two cameras, each with an adjustable distance to its tube lens, allowing independent control of the focal plane of each camera. Camera 1 is focused on dorsal cortex while camera 2 is focused on the entorhinal cortex, as imaged through a microprism and typically ~3 mm deeper than the first imaging plane.

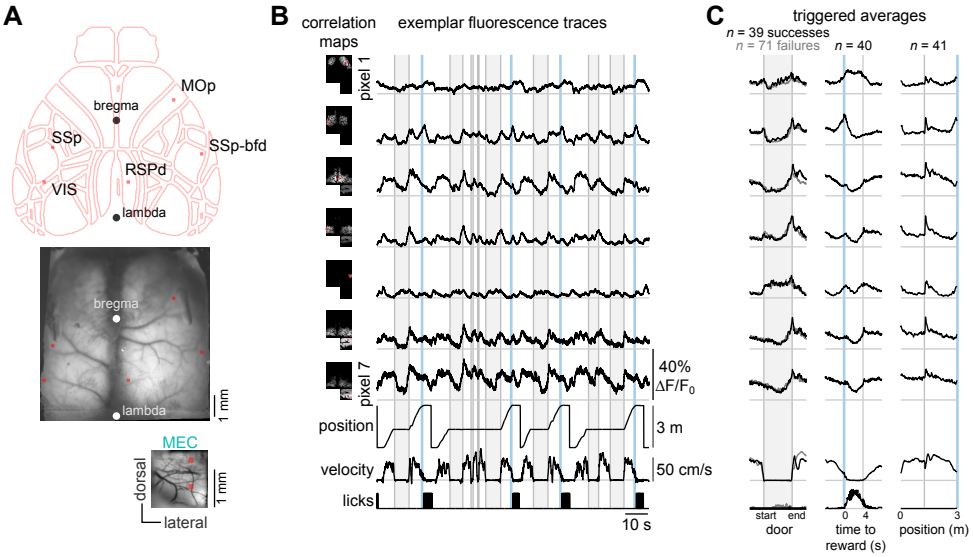

Figure 2. Brainwide Ca^{2+} signals during multi-component behavior

A) Mean fluorescence images acquired by two cameras, one focused on and cropped to the ~8 mm window over dorsal neocortex and the other to medial entorhinal cortex (MEC). Exemplar pixels to be scrutinized in next panels are indicated by red dots. Movies are registered to bregma and lambda, enabling alignment to the 2D "flatmap" of the Allen Mouse Brain Common Coordinate Framework[29].

B) Fluorescence signals shown for a 2-minute period for the seven exemplar pixels, with behavior underneath. Thumbnails show correlation maps between each pixel and the remaining image.

C) Triggered averages for the seven exemplar pixels and for velocity and licking with respect to the timing period at the door, the time to reward, and track position. For the timing period, time was normalized to the start and end of each wait attempt; further, trials were split into successes (wait time greater than the target time, which here was 6 s; dark trace) and failures (wait time greater than 2 s but less than the target time; gray trace). For time to reward, the teleportation back to the start of the track happens at 4 s, as indicated by the thin vertical gray line. For track position, only times when the velocity is positive are used; signals are resampled to 1-cm bins.

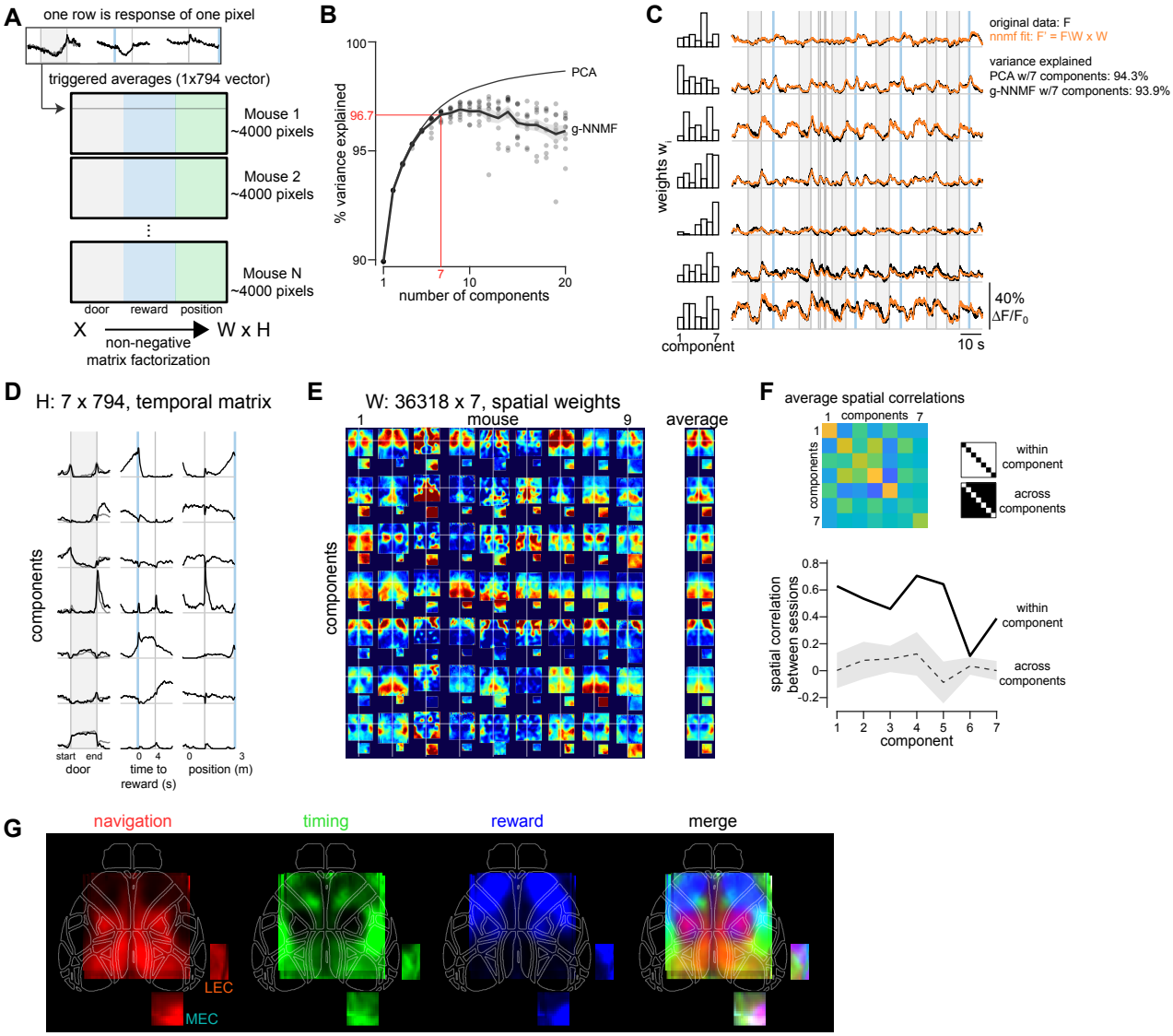

Figure 3. Isolation of task-relevant components using groupwise non-negative matrix factorization

A) A multi-session matrix X is formed for all pixels across nine sessions (each from a different mouse). Each row corresponds to the triggered average of a single pixel, formed by concatenating triggered averages for timing, reward, and track position as shown in Figure 2C.

B) Variance explained by non-negative factorization as a function of the number of components. Dots represent the 10 repeats for a given number of components; solid line and gray represent mean and standard error. For comparison, variance explained as a function of number of components is shown for principal component analysis (PCA).

C) Weights (left) and reconstruction (right, in orange) using non-negative factorization with seven components is shown for the exemplar traces from Figure 2B.

D) Temporal matrix H for the non-negative factorization of matrix X into H and W.

E) Spatial weights W for the non-negative factorization. These are reshaped as 2D spatial maps for individual sessions, which are aligned to bregma. Mean weights (averaged across sessions) are shown as well.

F) Spatial correlation between pairs of spatial weights for individual components and sessions, averaged either within component (same component, different sessions) or across components (different components, different sessions).

G) Mean spatial maps across multiple components. Navigation: components 2, 3, and 6; timing: component 7; reward: components 1 and 5. Averages are across nine sessions (eight for MEC, one for LEC).

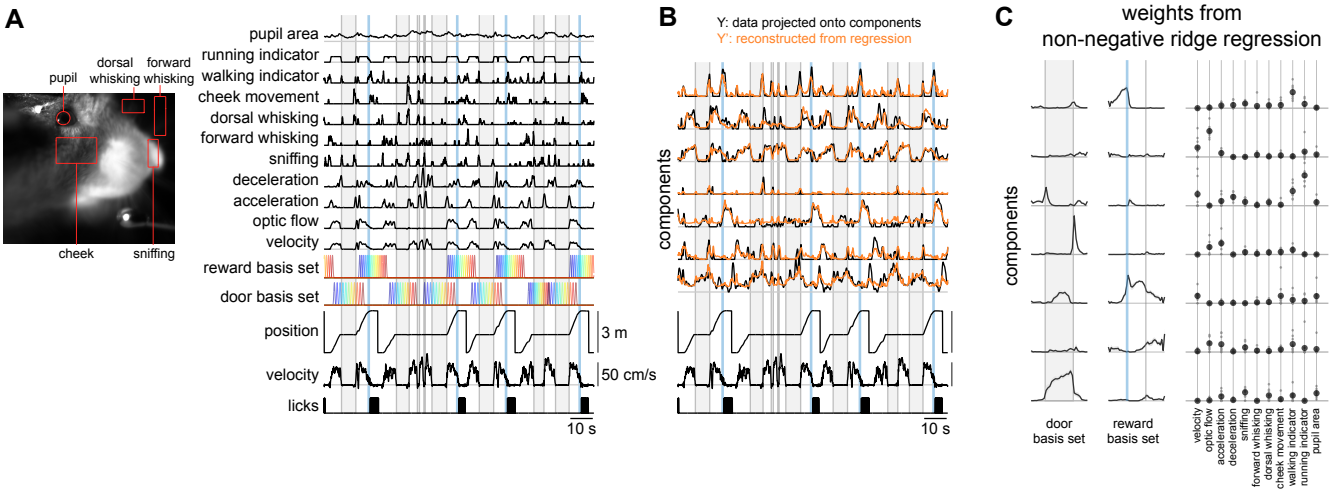

Figure 4. Relation of ongoing behavior to individual components

A) Predictors to be used for non-negative ridge regression, shown for the same exemplar period shown in Figure 2B. These include a door basis set and a reward basis set, formed by a set of indicator functions at different temporal shifts, here represented by different colors. Behavior predictors are computed from the treadmill velocity (velocity, optic flow, acceleration, deceleration, walking indicator, and running indicator) and from the movie of the mouse's face (sniffing, forward whisking, dorsal whisking, cheek movement, and pupil area).

B) Exemplar traces, projected onto the seven components from Figure 3, along with fit by non-negative ridge regression.

C) Weights from non-negative ridge regression for the predictors shown in A, averaged across nine sessions.